JPhys Photonics

PURPOSE-LED PUBLISHING™

PAPER • OPEN ACCESS

Sub-wavelength terahertz imaging using asynchronous optical sampling of on-chip near-field sensors

To cite this article: Connor D W Mosley *et al* 2026 *J. Phys. Photonics* **8** 025049

Journal of Physics: Photonics

Check for updates

OPEN ACCESS

RECEIVED
21 April 2026

REVISED
27 May 2026

ACCEPTED FOR PUBLICATION
8 June 2026

PUBLISHED
26 June 2026

PAPER

Sub-wavelength terahertz imaging using asynchronous optical sampling of on-chip near-field sensors

Connor D W Mosley[1,*], Joshua P R Nixon[1], Adam G Metcalf[1], Thomas B Gill[1], SaeJune Park[2], Lianhe Li[1], Christopher D Wood[1], Dominic Jones[1], Edmund H Linfield[1], A Giles Davies[1], Pietro Valdastri[1] and John E Cunningham[1]

[1] School of Electronic and Electrical Engineering, University of Leeds, Leeds LS2 9JT, United Kingdom
[2] School of Electronic Engineering and Computer Science, Queen Mary University of London, London E1 4NS, United Kingdom
[*] Author to whom any correspondence should be addressed.

E-mail: c.mosley@leeds.ac.uk

Keywords: terahertz, sensing, imaging, asynchronous optical sampling, time-domain spectroscopy

Supplementary material for this article is available online

Abstract

We demonstrate a near-field terahertz (THz) imaging modality based on asynchronous optical sampling of on-chip THz sensors, and apply it to the sub-wavelength imaging of silicone soft-tissue phantoms. The sensor consists of a planar Goubau-line waveguide that incorporates a quarter-wavelength stub band-stop resonator, with photoconductive switches integrated into the waveguide for broadband THz signal generation and detection. By raster-scanning soft-tissue phantoms through the evanescent electric field above the resonator using a robotic manipulator, we reconstruct two-dimensional THz images with spatial resolution down to 50 μm—more than one order of magnitude below the free-space wavelength at the operating frequency (355 GHz) - and with pixel acquisition times down to 100 ms. Image contrast is obtained using both frequency shifts of the resonator and changes in power transmission through the device, enabled by the broadband nature of the on-chip system. These results simultaneously establish the potential of on-chip near-field THz sensors as a platform for high-resolution imaging of soft tissue analogues, while also highlighting their potential for future applications in biomedical imaging and real-time sensing.

1. Introduction

Terahertz (THz) radiation has emerged as a promising candidate for applications in biomedical sensing and imaging [1–4], due to its non-ionising properties (having typical photon energies of several meV) and high sensitivity to biomarkers such as tissue water content. Free-space THz time-domain spectroscopy (THz-TDS) [5, 6] is a well-established technique for measuring material properties at THz frequencies, and has been widely applied in the study of condensed matter systems, in addition to biomedical applications. THz-TDS has demonstrated particular promise in the identification of cancerous tissue, such as in the skin [4, 7–10], breast [11, 12], and colon [13]. Additionally, THz-TDS has been used in the identification of skin pathologies such as burns [14] and diabetic foot syndrome [15]. However, THz applications in biomedical sensing and imaging have so far been mostly limited to external, surface-based conditions or *ex vivo* samples due to several challenges faced by free-space THz-TDS systems: a diffraction-limited spatial resolution, strong absorption by atmospheric water vapour, and free-space THz optics are typically large and cumbersome. Additionally, all THz sensing and imaging techniques must contend with the limited penetration depth of THz radiation in biological tissue (several 100 μm in skin, for example).

A potential solution to some of these challenges can be provided by on-chip THz-TDS techniques [16], in which the evanescent field surrounding on-chip THz waveguides is utilised to perform spectroscopic measurements. On-chip THz-TDS devices do not require an atmosphere purged of water vapour, the active region of the devices are small (typically under several mm^2), and they have the potential to measure material properties on length scales below the diffraction limit [17, 18]. Recent simulations of on-chip THz sensors have highlighted their potential for applications in imaging of colon cancer tumour margins [19] and for general dielectric sensing [20]. The compact nature of on-chip THz devices offers the potential for integration into existing *in vivo* diagnostic equipment, such as colonoscopy probes, providing a route to THz imaging inside the human body. Several planar waveguide geometries have been investigated for on-chip THz-TDS devices, including microstrip line [21], coplanar waveguide (CPW) [22], and planar Goubau line (PGL) [23]. Of these, the larger evanescent field extent of the PGL [24] positions it as the most promising system for sensing, owing to its stronger interaction with overlaid materials. However, no prior experimental studies have investigated PGL on-chip sensors for THz imaging. Additionally, on-chip THz-TDS measurements have so far been constrained to solid [17, 25], polycrystalline [21, 26], or microfluidic samples [27], with their applicability to the biosensing of soft tissue so far being unexplored. Phantoms, i.e. materials that mimic the mechanical and/or optical properties of biological tissue, are commonly used in experimental testing techniques for biomedical applications. Various biological phantom materials have been reported in the literature, including polyvinyl alcohol, copolymer in oil, silicone, polyurethane, epoxy resin, and aqueous suspensions [28, 29]. At THz frequencies, gelatine- or agar-based gels are often used to create phantoms [30, 31], though these materials degrade over time and require special storage conditions to prevent water evaporation. Here, we fabricate phantoms from commercially-available silicone, mainly to exploit its excellent stability over time and mechanical properties, which mimic soft tissue [28, 29].

In this work, we present the design, simulation, and experimental validation of an on-chip near-field THz sensing system using a PGL. We designed the sensor to operate at a nominal centre-frequency of 360 GHz, within the region of high dynamic range for a typical on-chip THz-TDS system [22]. The sensor was sampled using an asynchronous optical sampling (ASOPS) laser system; ASOPS THz-TDS is a well-established technique in free-space systems [32], and offers the potential for fast THz-TDS measurements of on-chip systems [22]. We demonstrate use of this system to create raster-scanned THz images of a silicone soft-tissue phantom mounted on a robotic manipulator, showing its ability to resolve features well below the free-space diffraction limit at the device's operating frequency, with per-pixel data acquisition times as short as 100 ms.

2. Sensor design and simulation

Figure 1(a) presents an optical micrograph of the on-chip sensor developed during this work, which was fabricated on a quartz substrate using the method described previously [22] and mounted onto a bespoke printed circuit board (PCB). The device comprises two regions of CPW used to launch and detect THz signals into the device. The CPW design includes a 30 μm-wide centre conductor positioned between two ground planes, each separated by a 20 μm gap. Sandwiched between the two CPW sections is a 5 μm-wide, 800 μm-long PGL which forms the sensing region of the device. The PGL was curved through an angle of 130° to spatially isolate the sensing region from the rest of the device, minimizing possible parasitic interactions between an analyte and non-sensing regions of the waveguide. Excitation and detection of broadband THz signals is achieved using a pair of photoconductive switches (PCS) integrated into the waveguide at either end of the PGL, and beneath the CPW to PGL transitions. The PCS were formed from regions of low-temperature grown gallium arsenide (LT-GaAs) epitaxially-transferred [23] onto the quartz substrate beneath the overlaid waveguide, as shown in figure 1(b). Each PCS may be used individually to generate or detect THz signals in the device. The PCS includes voltage and current probe arms, required to inject and detect THz signals, positioned orthogonally to the centre conductor of the CPW and separated by a 5 μm gap, allowing a CPW waveguide mode to be excited efficiently within the structure under optical excitation. The CPW mode is then coupled into a radial Goubau mode within the PGL via impedance transformation, using a parabolic horn antenna design [23] in which the centre conductor of the CPW was tapered down to match width of the PGL, whilst simultaneously flaring out the ground planes to establish a radial electric field. CPW was chosen for the generation and detection regions as the integrated ground planes minimise cross-coupling between either side of the device (such as between V_2 and D_1 in figure 1(a)). At the centre of the PGL, a 130 μm-long, 5 μm-wide QWS band-stop resonator is positioned and used for sensing. The QWS inverts the phase of a portion of a THz pulse propagating along the transmission line, causing destructive interference and therefore attenuation of the pulse across a narrow band of frequencies centred on $f_0 = c/4l\sqrt{\epsilon_{\mathrm{eff}}}$, where c is the speed of light in vacuum, l is the length of the QWS, and ϵ_{eff} is the effective permittivity of the

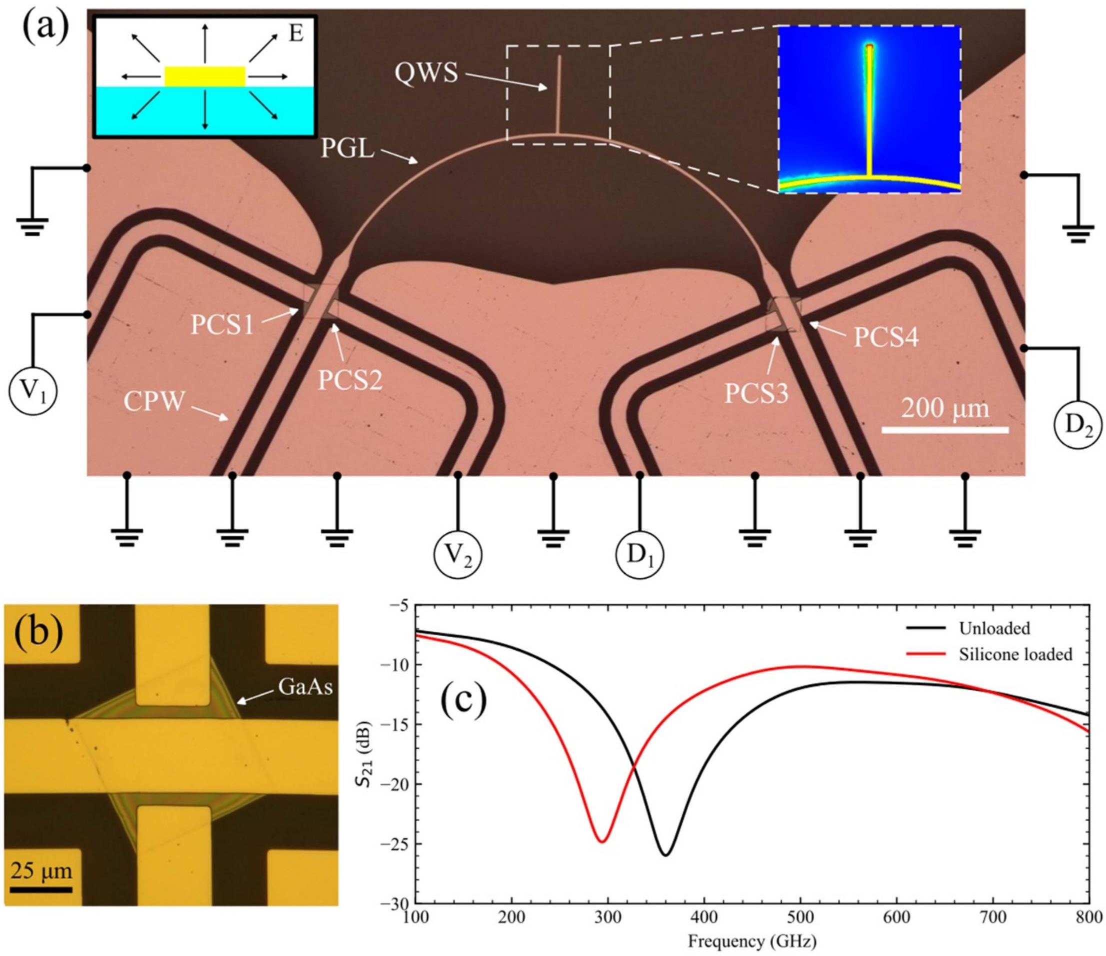

Figure 1. (a) Optical micrograph of the on-chip THz sensor, with electrical connections labelled. The metallized waveguide structure is shown by the lighter orange sections, while the substrate is seen as the dark brown background. Inset at the top left is a schematic diagram depicting the Goubau mode around the PGL. Inset at the top right is the on-resonance electric field around the quarter wave stub (QWS) extracted from finite-element simulations using HFSS. (b) Optical micrograph showing one set of integrated photoconductive switches, with the LT-GaAs layer visible as a light grey patch underneath the metallization. (c) Forward transmission parameter S_{21} of the sensor when unloaded (black line) and loaded with silicone (red line).

surrounding medium. The presence of an analyte positioned within the evanescent field of the QWS will alter the effective dielectric permittivity, causing a shift in the resonant frequency of the device.

Finite-element simulations of the device were performed using commercial 3D electromagnetic simulation software (Ansys HFSS). Two-port S-parameter simulations were carried out in the frequency range 100 GHz–800 GHz, with the simulation model including the 800 μm-long curved section of the PGL with integrated QWS resonator. The forward transmission parameter S_{21} of the device, with no analyte present, is shown by the black line in figure 1(c) in which a single resonance was observed at the central design frequency of $f_0 = 360$ GHz. The in-plane electric field distribution around the QWS at f_0 is displayed in the inset of figure 1(a), showing that the field strength is highest at the tip of the QWS and decays closer to the PGL, as expected for a quarter-wave resonator. To simulate the interaction of the sensor with a silicone phantom accurately, the THz optical properties of silicone were first determined using free-space THz-TDS transmission measurements of a 10 mm by 10 mm, 2.47 mm-thick slab of material (see supplemental document for details). The broadband relative permittivity ϵ_r and dielectric loss tangent $\tan\delta$ extracted from these measurements were used to model the frequency-dependent dielectric properties of silicone in HFSS. Values of $\epsilon_r = 3.36$ and $\tan\delta = 0.075$ were obtained at 360 GHz, for reference; this dielectric permittivity is between that of fibrous and fatty human breast tissue ($\epsilon_r \approx 3.9$ and 2.4 at 360 GHz, respectively) [11], and comparable to calculations of human skin with low (approx. 30%) levels of hydration [15]. Next, a 150 μm-thick, 500 μm by 500 μm block of silicone, centred on the QWS and in contact with the top surface of the gold, was introduced into the simulation and two port S-parameter simulations were repeated, shown by the red line in figure 1(c). The resonant frequency of the sensor is observed to have shifted down to 295 GHz, representing a change in resonant frequency of 65 GHz.

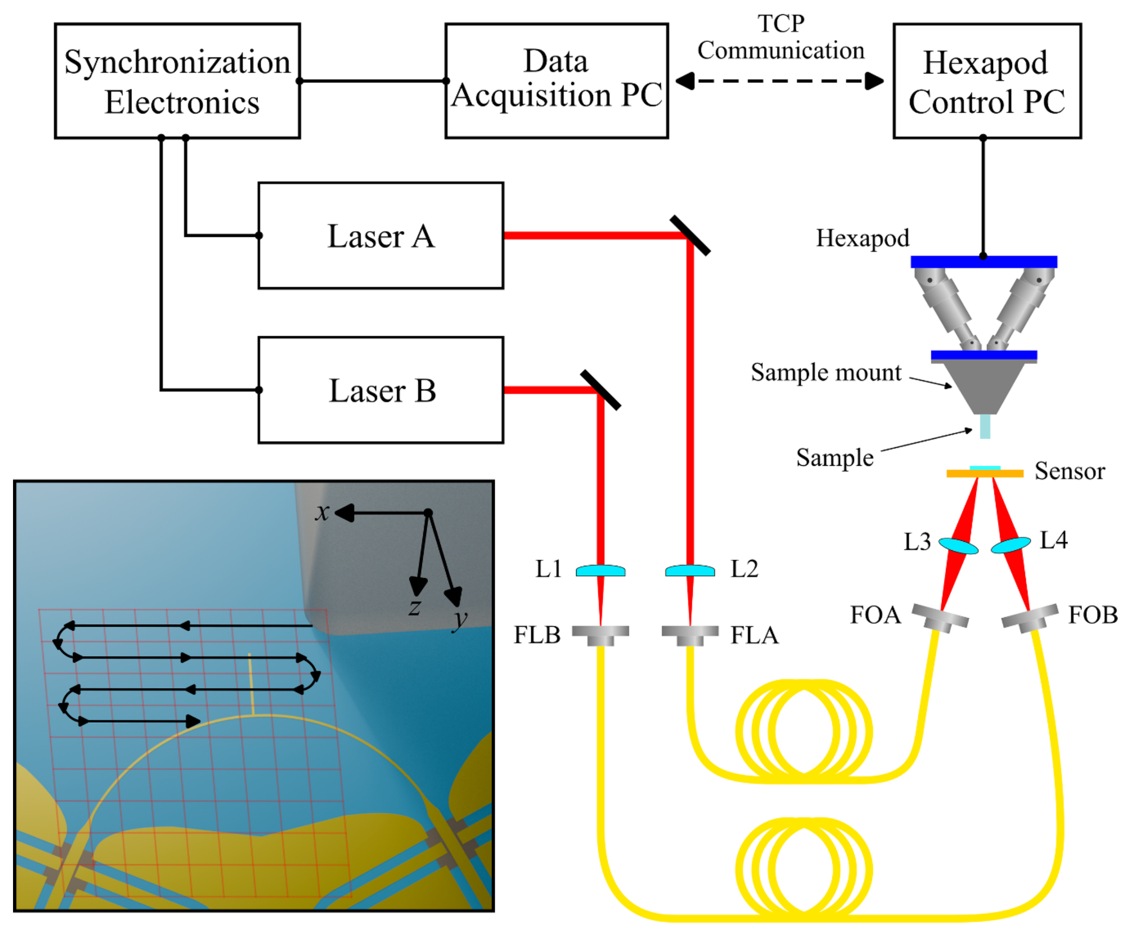

Figure 2. Schematic diagram of the experimental setup used in this work. L = lens, FL = fibre launch, FO = fibre output. Inset is a schematic diagram depicting the sample being moved in a grid pattern relative to the sensor to create a rasterized THz image.

3. Experimental methods

3.1. Experimental arrangement

A schematic diagram of the optical arrangement used in this work is shown in figure 2, which was designed to mimic the layout required for future applications of on-chip THz sensors in biomedical imaging; incorporating the sensor into a flexible endoscope, for example, would require beam delivery to the chip via optical fibres with the lasers focused through the substrate onto the PCS, both of which we demonstrate here. A commercially-available ASOPS laser system (Menlo Systems) was used, which consisted of two ultrafast lasers (laser A and laser B, C-Fiber 780) each producing < 100 fs-duration pulses with 780 nm centre wavelength and an average optical power of 50 mW. The output of laser A and laser B were each coupled into a 2 m-long hollow-core photonic crystal (HCPC) optical fibre (GLOphotonics HCPCF-850-60) using 50 mm focal length lenses (L1 and L2). These HCPC fibres were used due to their low dispersion at our central laser wavelength of 780 nm [33]. The pulse duration of the lasers was measured using a commercial autocorrelator (APE pulseCheck), yielding a pulse duration of 78 fs, which increased to 110 fs after propagation along the HCPC fibre. At the fibre output, divergent light from the bare fibre end was collected and focused onto the device a pair of 38 mm focal length lenses (L3 and L4), each arranged in a 4*f* configuration between the fibre end and the device. The large mode field diameter of the fibre (45 ± 3 μm at 780 nm [33]) resulted in all emitted laser light being captured by the lenses owing to the limited beam divergence. The optical power delivered to the chip was measured as 32 mW for laser A and 29 mW for laser B, using a calibrated photodiode sensor (Thorlabs S121C), with the difference likely due to individual fibre input coupling efficiency or alignment. A 5 mm-diameter through-hole in the PCB allowed the optical pulses to be focused through the rear of the quartz substrate, and then aligned to the PCS using *x*–*y*–*z* translation mounts on the fibre outputs and lenses. Coarse alignment was performed by observing the laser position on the chip using a CMOS camera, followed by fine alignment achieved by optimizing the measured photocurrent across each switch, supported by real-time observation of the measured THz waveform.

ASOPS THz-TDS measurements of the sensors were performed by operating laser A at a constant repetition rate of 100 MHz, whilst laser B was operated at a slightly different repetition rate of 100 MHz $+\ \Delta f$. The repetition rate difference $\Delta f = 10$ Hz, providing a balance between experimental bandwidth and fast measurements. A constant voltage of +20 V DC was applied to both V_1 and V_2 (figure 1(a)) to create a symmetric electric field on either side of the CPW center conductor. A THz pulse was then generated and launched into the waveguide by simultaneous photoexcitation of PCS1 and PCS2 using laser A. After propagation along the PGL, the THz pulse was detected in a time-gated manner by photoexcitation of PCS3 using laser B and sampling the induced current at D_1. The device layout permits detection at either D_1 or D_2, providing detection redundancy; however, here we present data only from D_1 for consistency. The photocurrent signal from D_1 was converted into a voltage and amplified using a transimpedance amplifier (Femto DHPCA-100), with data capture performed using a fast analogue-to-digital converter in the data acquisition PC.

3.2. Phantom preparation

A mold for the phantoms was designed in Fusion360 and then 3D printed (Formlabs Form 3, grey resin). The 3D print was then washed in isopropanol and cured for 30 min at 60 °C , followed by a second washing step and bake at 150 °C to ensure that all the resin was cured and thereby ensure complete curing of the silicone casting agent. A platinum cure silicone (Smooth-On Inc. EcoFlex 00-30) was degassed and blended using a vacuum mixer (THINKYMIXER ARV-310). This was then injected into the mold and left to cure at 50 °C for 24 h. The phantom was then released from the mold and subjected to an additional 24 hour cure at 50 °C. Finally, the phantom was washed with isopropanol to remove any residual uncured silicone.

3.3. Phantom scanning

Translation of phantoms relative to the chip was achieved using a hexapod robotic platform (Symetrié SOLANO), with a linear travel range of 18 mm and a resolution of 100 nm in the *x*-*y* plane (parallel to the surface of the chip), and a linear travel range of 6.5 mm and a resolution of 80 nm in the *z*-axis (height above the chip). The silicone phantoms were mounted at the tip of a 3D-printed probe head (Formlabs grey resin), which was attached to the top plate of the hexapod. The tip of the phantom was raster-scanned back and forth according to a programmable scan area and scan resolution (shown schematically in the inset of figure 2). The contact position, i.e. when the phantom makes contact with the device, was calibrated using a force sensor mounted behind the phantom in conjunction with monitoring the THz response of the device. During the scanning procedure, the tip of the phantom was introduced to the sensor, data acquisition performed, and then the phantom was withdrawn by 250 μm, ensuring that there was no contact between the phantom and the chip during lateral movement of the hexapod. The phantom was then moved to the next raster point and introduced back into contact for subsequent data acquisition. This process was repeated until the full raster scan had completed.

4. Experimental results & discussion

4.1. Real-time data acquisition from on-chip sensors

To characterize the device operation, its unloaded response (i.e. with no sample in contact with the sensor) was first measured. Figure 3(a) presents THz time-domain waveforms, obtained using ASOPS, for a range of acquisition times between 100 ms and 100 s. With our chosen repetition rate difference of $\Delta f = 10$ Hz, a single time-domain waveform can be acquired in only 100 ms, shown by the yellow trace in figure 3(a), demonstrating the ability of the system to provide real-time data acquisition. The 1 s (pink), 10 s (purple), and 100 s (blue) traces in figure 3(a) represent the average of 10, 100, and 1000 individual time-domain waveforms, respectively. The maximum amplitude of the waveform remains constant across all acquisition times, with longer acquisition times having reduced noise. The corresponding Fourier-transformed power spectra of the waveforms in figure 3(a) are presented in figure 3(b). A 70 ps-wide Hann window centered at 0 ps (on the peak of the THz pulse) was applied to each waveform before Fourier transformation, resulting in a frequency resolution of 14.28 GHz. The width of the Hann window was determined by the position of the first time-domain reflection of the THz signal, arising from the nearest wire-bond used to interface with external hardware, measured at a time delay of 50 ps. A 15 dB resonance can be observed in the power spectra at 355 GHz for all measurements, in good agreement with the design frequency of 360 GHz the QWS resonator. The difference of 5 GHz between experiment and simulation is likely caused by fabrication tolerances or slight differences

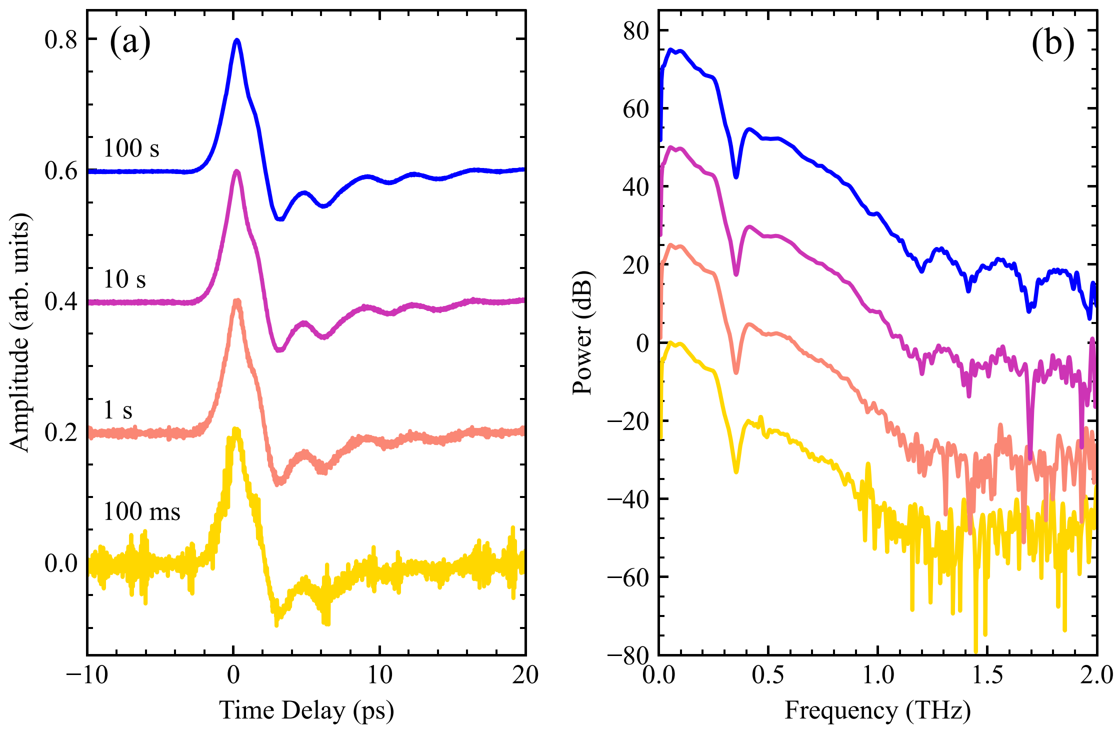

Figure 3. (a) THz time-domain waveforms obtained from the unloaded on-chip sensor as a function of acquisition time (indicated to the left of each waveform). Waveforms are offset vertically for clarity. (b) Corresponding power spectra of the time-domain waveforms in panel (a). Spectra are offset vertically for clarity.

in material properties between simulation and experiment. Furthermore, the data show that a single scan is sufficient to clearly resolve the QWS resonance, confirming that high-speed acquisition can be applied without compromising the usability of the measured signal.

4.2. Sensor response to silicone phantoms

The sensing capabilities of the device were next characterized by observing the shift in sensor resonant frequency upon interaction with a 1 mm by 1 mm, 500 μm-thick silicone phantom, shown in figure 4(red trace) compared with the unloaded resonance of 355 GHz (black trace). Both traces are the average of 100 individual THz pulses (corresponding to an acquisition time of 10 s). The resonant frequency was seen to decrease when the sensor was in contact with the silicone, shifting down by 57 GHz to 298 GHz, in good agreement with the simulated value of 295 GHz. As in the unloaded case, the small difference between experiment and simulation may be due to fabrication tolerances or slight differences in material properties; additionally, a small gap (on the order of 1 μm) introduced by air being trapped between the phantom and sensor could cause the experimentally measured frequency shift to be lower than the simulation [16]. The minor oscillations either side of the main resonance may be a characteristic feature of the device response, and may be investigated by future simulations that include the entire device design (for instance, the horn coupling sections). The time-domain waveforms corresponding to the loaded and unloaded device spectra are presented in the inset of figure 4. We investigated the reproducibility of the silicone phantoms by repeating the measurements in figure 4 with two additional independently fabricated silicone phantoms (see supplemental document for details). The resonant frequency of the silicone-loaded sensor had a range of 1.42 GHz and a mean of 297.5 GHz for the three measurements, demonstrating that the results are reproducible between different silicone phantoms.

In practical biosensing applications, for example determining colorectal cancer tumour margins, a sensitivity to changes in relative permittivity of around 1 is required in order to discriminate between healthy ($\epsilon_r \approx 5$) and cancerous ($\epsilon_r \approx 6$) colon tissue [19]. The sensitivity S of our device can be calculated from $S = \Delta f_0/\Delta n$ [20], where Δf_0 is the change in resonant frequency of the device between measurements of two analytes with a change in refractive index of Δn, which may be calculated from their relative permittivities as $\Delta n = \sqrt{\epsilon_{r,1}} - \sqrt{\epsilon_{r,2}}$. Using the data from figure 4, $\Delta f_0 = 55$ GHz and $\Delta n = 0.83$ between air and silicone, resulting in a sensitivity $S = 66$ GHz/RIU (where RIU = refractive index unit). With this sensitivity, our device would produce a frequency shift of around 14 GHz for a change in

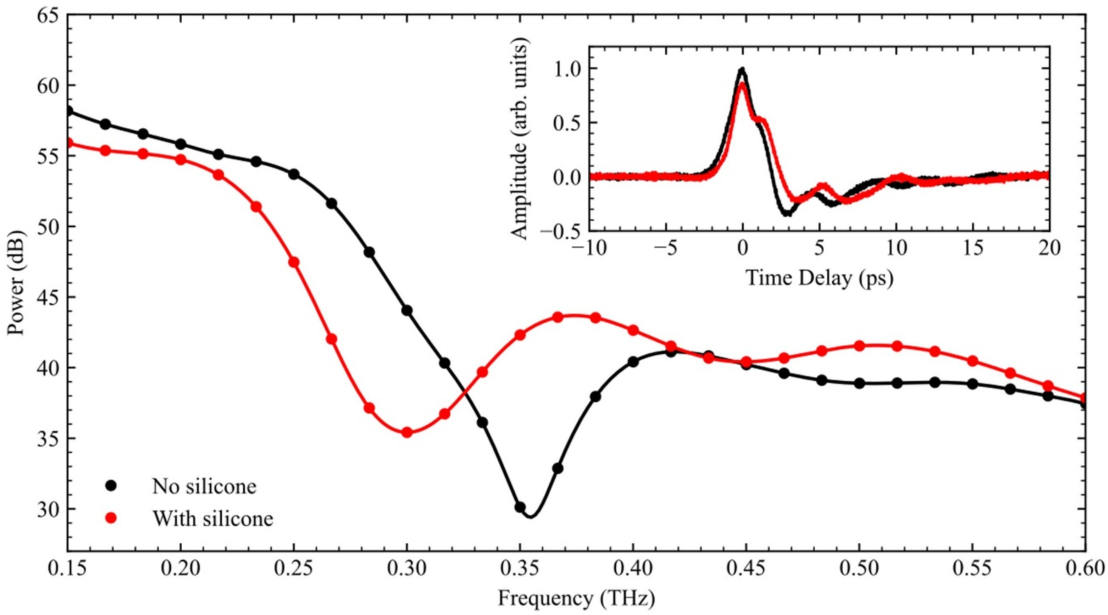

Figure 4. Response of the on-chip sensor while unloaded (black data) and loaded with silicone (red data). Dots show the raw data after Fourier transforming the time-domain waveforms, and lines show data obtained by zero-padding the time-domain waveforms before Fourier transforming. Inset are the time-domain data corresponding to the spectra in the main figure; each trace is the average of 100 individual time-domain waveforms.

relative permittivity from 5 to 6, comparable to the 14.28 GHz frequency resolution of our sensing system. The sensitivity of the device presented here is comparable to that found in experimental measurements of metamaterials for THz sensing (70 GHz/RIU [34]), and simulations of split-ring resonators (64 GHz/RIU [19]) and QWS (85 GHz/RIU [20]) coupled to Goubau lines, with the small discrepancy between the simulations of [20] and our device potentially due to the simulation's use of perfect electrical conductors rather than gold. The precision to which we can measure the resonant frequency of our devices was estimated by constructing a histogram of the measured resonant frequency from 1000 repeat measurements (see supplemental document for details). The standard deviation of this distribution is 1.2 GHz, hence the system has a 3σ precision of 3.6 GHz—more than sufficient to resolve the difference between healthy and cancerous colon tissues.

4.3. Imaging silicone phantoms using on-chip sensors

To verify the imaging capability of our sensor, a patterned silicone phantom was raster-scanned over a 1.5 mm by 1.5 mm range around the on-chip sensor, with a step (pixel) size of 50 μm in both the x- and y-directions. The 50 μm spatial resolution of the scan is an order of magnitude smaller than the free-space wavelength at the operating frequencies of the device (844 μm for a frequency of 355 GHz) and was limited here only by the chosen x and y step size, selected purely for convenience. An optical micrograph of the phantom is presented in figure 5(a), which was a 1.4 mm by 1.3 mm wide, 2.1 mm-long, flat-top pillar of silicone cast in a bowtie shape, with the tapered sections of the bowtie having a depth of 270 μm and an angle of 95°. The scan origin was chosen by setting the bottom left hand corner of the phantom 200 μm above (in y) and 200 μm to the right (in x) of the tip of the QWS (pictured schematically in the inset of figure 2). Two sets of measurements were taken, with different data acquisition times per pixel. In the first measurement, for each pixel of the image, 100 individual THz-TDS waveforms were recorded and then averaged, corresponding to a total acquisition time of 10 s per pixel. In the second measurement, the same raster pattern was repeated but with only a single THz-TDS waveform recorded at each pixel, corresponding to an acquisition time of 100 ms per pixel. Figure 5(b) illustrates two available methods for image reconstruction from the measured signals, using either: the change in resonant frequency of the device (Δf); or the change in the value of the THz power spectrum at a specific frequency (ΔP). A 70 ps-wide Hann window was applied to the THz waveform recorded at each pixel before Fourier transforming to obtain the frequency spectra. Next, the power spectrum between 100 GHz and 600 GHz at each pixel was fit by a Lorentzian function plus a linear term to account for the underlying slope of the spectrum, and the resonant frequency of the device was obtained by extracting the central frequency of the Lorentzian.

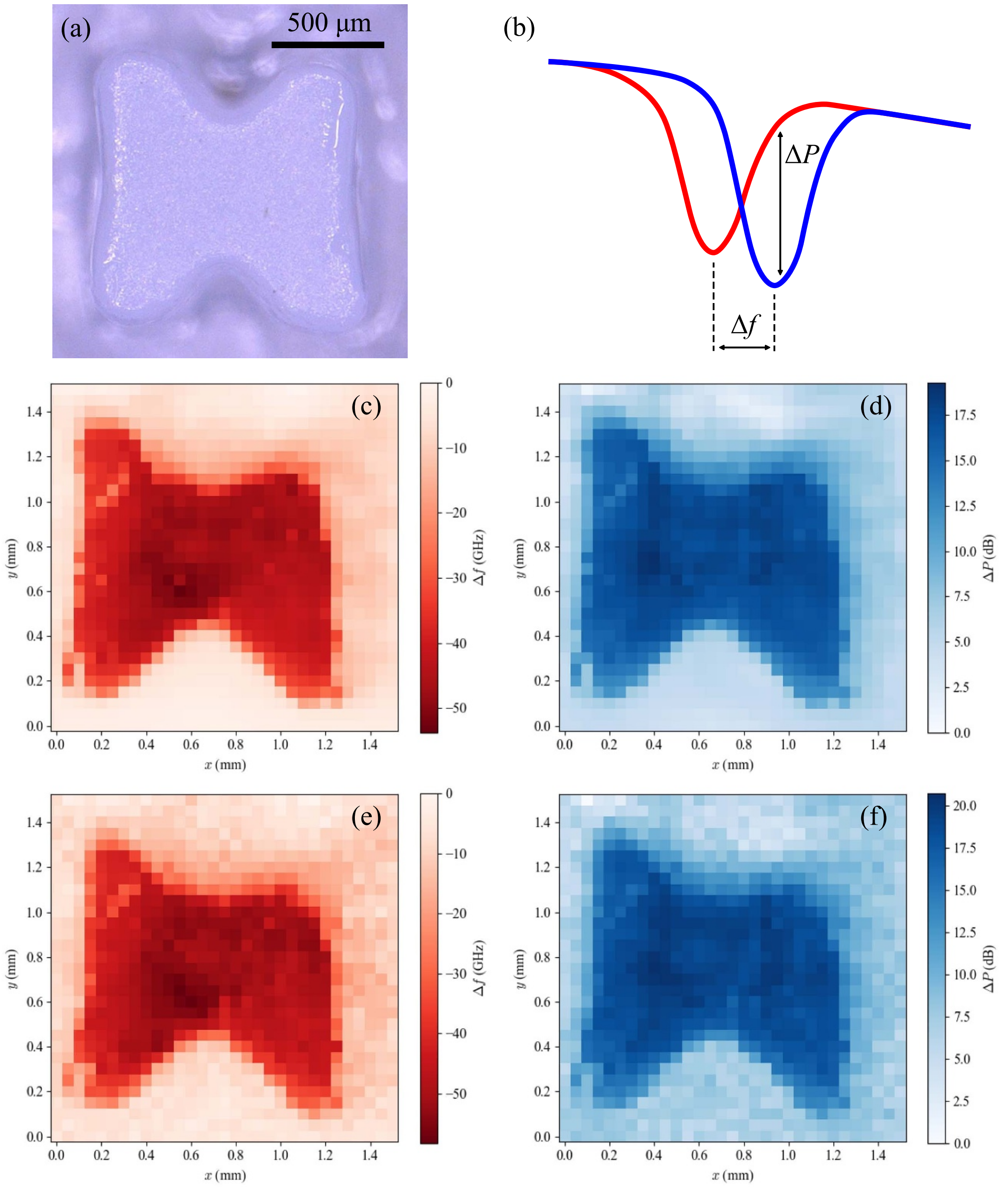

Figure 5. (a) Optical micrograph of the silicone phantom used in the imaging raster scans. (b) Schematic diagram demonstrating two imaging contrast mechanisms with the sensor data, observing the frequency shift of the QWS resonance (Δf), or by observing the change in power at a given frequency (ΔP). Panels (c) and (e) show raster-scanned THz images of the silicone phantom obtained using Δf, with per-pixel acquisition times of 10 s and 100 ms, respectively. Panels (d) and (f) show raster-scanned THz images of the silicone phantom obtained using ΔP at 357 GHz, with per-pixel acquisition times of 10 s and 100 ms, respectively.

Figures 5(c) and (e) present the change in resonant frequency Δf of the on-chip sensor at each position in the raster scan, for pixel acquisition times of 10 s and 100 ms, respectively. A clear image of the silicone phantom can be observed in the resonant frequency response of the sensor, which is in excellent agreement with the shape of the phantom in the optical image from figure 5(a). The resonant frequency is observed to decrease by up to 55 GHz when the silicone phantom is overlaid on the QWS, in agreement with the bulk silicone measurement presented in figure 4, and returns to the unloaded value in areas where the silicone phantom is not in contact with the sensor. Figures 5(d) and (f) show the change in the value of the THz power spectrum at 357 GHz at each position in the raster scan, for pixel acquisition times of 10 s and 100 ms, respectively. We choose 357 GHz as it is slightly higher than the resonant frequency of the unloaded device, hence will show a monotonic increase in transmitted power as the resonance downshifts upon loading with silicone. As before, a clear image of the phantom can be observed in the sensor response which is in excellent agreement with the shape of the optical image in figure 5(a). This method has the added bonus of being extracted from the raw data points of the Fourier transformed spectra, hence not relying on a background subtraction or fitting to extract values.

The THz images in figures 5(c) and (f) will be a product of the shape of the phantom and the physical size of the QWS resonator, resulting in a different theoretical minimum spatial resolution in the x- and y-directions; the y-resolution is limited to approximately 100 μm by the length of the QWS, whilst the x-resolution may be as small as 5 μm due to the width of the QWS, and instead is constrained here by the chosen raster step size. The achievable spatial resolution may be improved in future work using several methods: reducing the QWS length, with the trade-off of a higher resonant frequency hence a decrease in measurement dynamic range; reorienting the sample and resonator by 90° to utilise the higher resolution provided by the width of the QWS, with the trade-off of increased imaging time; by using different resonant elements, such as split-ring resonators, which may localise the field in a more uniform area [20]; and by coupling multiple resonant elements to the same waveguide, as simulated in [35].

For the images presented in figure 5, the total image acquisition time was 3.2 h. The images consist of 961 raster points, with a wait time of 10 s per pixel applied in all raster scans to isolate the impact of the ASOPS acquisition time on image quality. The time taken for the hexapod to move from one raster position to the next and settle was 2 s; this constitutes a velocity of approximately 275 $\mu\mathrm{m\,s^{-1}}$, which is significantly slower than the maximum velocity of the hexapod, $v^{xy}_{\mathrm{max}} = 30\ \mathrm{mm\,s^{-1}}$ and $v^{z}_{\mathrm{max}} = 20\ \mathrm{mm\,s^{-1}}$ [36]. As such, the time taken to move between raster points could potentially be reduced by nearly two orders of magnitude, and an equivalent raster scan to that presented in figure 5(e) could theoretically be completed in as little as several minutes. Future work may experimentally investigate faster scanning and its impact on image quality. Scan acquisition time may be further improved by higher ASOPS acquisition rates, or by removing the requirement for the z-retraction of the sample; this may potentially be achieved by coating the chip in a thin protective layer of material, for instance Parylene C [37], which is biocompatible and may be applied in μm-thick layers using standard techniques, which would minimise the impact on device sensitivity.

5. Conclusions

In this work, we have demonstrated THz imaging of soft tissue phantoms using an on-chip, near-field sensor. The device design was presented, with finite-element simulations demonstrating the ability to sense overlaid dielectric media using the shift in its resonant frequency. We demonstrated real-time acquisition of THz-TDS data from the device using an ASOPS laser system, with the sensor's resonant response clearly visible in spectra acquired in as little as 100 ms. The experimentally observed frequency shift upon loading the device with silicone was in good agreement with simulation. Using a robotic manipulator, we performed raster-scanned imaging of a patterned silicone phantom, accurately reproducing the shape of the phantom using the sensor response, achieving per-pixel data acquisition times of as little as 100 ms. Future work may explore coupling multiple resonators to a single waveguide, as simulated in [35], which could allow multi-frequency imaging and improve scanning times. Additionally, whilst in this work we move the sample around the sensor for simplicity, in future the fibre-to-chip optics may be mounted onto a robotic platform to allow the sensor to be moved instead. Future miniaturisation of the fibre-to-chip optics could allow the device to be mounted inside an endoscopy probe, for example the system presented in [38], opening a route to THz imaging inside the human body. Our results demonstrate the applicability of on-chip near-field THz sensors for high-speed dielectric sensing and high-resolution imaging, and our use of a soft-tissue phantom provides an initial proof-of-concept for the use of this sensing system in biomedical imaging; however, further studies are required to investigate the response of such sensors with real biological samples.

Acknowledgments

The authors would like to acknowledge training and support provided by Mark Rosamond, Rory Gilroy, and Rob Farr from the Leeds Nanotechnology Cleanroom. For the purpose of open access, the author has applied a Creative Commons Attribution (CC BY) licence to any Author Accepted Manuscript version arising.

Data availability statement

The data that support the findings of this study are openly available at the following URL/DOI:. https://doi.org/10.5518/1830 [39].

Funding

The authors gratefully acknowledge funding from the Engineering and Physical Sciences Research Council (EPSRC), grant numbers EP/V047914/1, EP/W028921/1, EP/V004743/1, and EP/Y018079/1.

Author contributions

C. D. W. Mosley: Investigation, Conceptualization, Methodology, Resources, Software, Formal Analysis, Data Curation, Visualization, Writing—original draft, Writing—review & editing, Project administration; J. P. R. Nixon: Investigation, Resources, Formal Analysis, Data Curation, Visualisation, Writing—review & editing; A. G. Metcalf: Investigation, Resources, Software, Methodology, Validation; T. B. Gill: Investigation, Resources, Formal Analysis, Data Curation, Visualization, Writing—review & editing; S. J. Park: Conceptualization, Writing—review & editing, Funding acquisition; L. Li: Resources; C. D. Wood: Resources, Writing—review & editing; D. Jones: Resources; E. H. Linfield: Resources, Funding acquisition; A. G. Davies: Resources, Funding acquisition, Writing—review & editing; P. Valdastri: Resources, Funding acquisition, Writing—review & editing, Project administration; J. E. Cunningham: Funding acquisition, Conceptualization, Writing—review & editing, Project administration.

ORCID iDs

Connor D W Mosley 0000-0002-0084-9261
Joshua P R Nixon 0009-0009-6529-7259
Adam G Metcalf 0009-0006-2394-9632
Thomas B Gill 0000-0002-1191-6466
SaeJune Park 0000-0001-8606-191X
Lianhe Li 0000-0003-4998-7259
Christopher D Wood 0000-0003-1679-5410
Dominic Jones 0000-0002-2961-8483
Edmund H Linfield 0000-0001-6912-0535
A Giles Davies 0000-0002-1987-4846
Pietro Valdastri 0000-0002-2280-5438
John E Cunningham 0000-0002-1805-9743

References

[1] Taylor Z D *et al* 2011 THz Medical Imaging: *in vivo* Hydration Sensing *IEEE Trans. Terahertz Sci. Technol.* **1** 201–19
[2] D'Arco A, Di Fabrizio M, Dolci V, Petrarca M and Lupi S 2020 THz pulsed imaging in biomedical applications *Condens. Matter* **5** 25
[3] Leitenstorfer A *et al* 2023 The 2023 terahertz science and technology roadmap *J. Phys. D: Appl. Phys.* **56** 223001
[4] Agarwal A and Pickwell-MacPherson E 2026 Past, present and future of *in vivo* THz skin sensing *J. Phys. Photonics* **8** 011001
[5] Koch M, Mittleman D M, Ornik J and Castro-Camus E 2023 Terahertz Time-Domain Spectroscopy *Nat. Rev. Methods Primers* **3** 48
[6] Jepsen P U, Cooke D G and Koch M 2011 Terahertz spectroscopy and imaging – Modern techniques and applications *Laser Photonics Rev.* **5** 124–66
[7] Woodward R M, Cole B E, Wallace V P, Pye R J, Arnone D D, Linfield E H and Pepper M 2002 Terahertz pulse imaging in reflection geometry of human skin cancer and skin tissue *Phys. Med. Biol.* **47** 3853
[8] Woodward R M, Wallace V P, Arnone D D, Linfield E H and Pepper M 2003 Terahertz pulsed imaging of skin cancer in the time and frequency domain *J. Biol. Phys.* **29** 257
[9] Woodward R M, Wallace V P, Pye R J, Cole B E, Arnone D D, Linfield E H and Pepper M 2003 Terahertz pulse imaging of ex vivo basal cell carcinoma *J. Investig. Dermatol.* **120** 72
[10] Fan B, Neel V A and Yaroslavsky A N 2017 Multimodal Imaging for Nonmelanoma Skin Cancer Margin Delineation *Lasers Surg. Med.* **49** 319–26

[11] Ashworth P C, Pickwell-MacPherson E, Provenzano E, Pinder S E, Purushotham A D, Pepper M and Wallace V P 2009 Terahertz pulsed spectroscopy of freshly excised human breast cancer *Opt. Express* **17** 12444
[12] Cassar Q *et al* 2021 Terahertz refractive index-based morphological dilation for breast carcinoma delineation *Sci. Rep.* **11** 6457
[13] Reid C B, Fitzgerald A, Reese G, Goldin R, Tekkis P, O'Kelly P S, Pickwell-MacPherson E, Gibson A P and Wallace V P 2011 Terahertz pulsed imaging of freshly excised human colonic tissues *Phys. Med. Biol.* **56** 4333
[14] Osman O B *et al* 2022 *In Vivo* Assessment and Monitoring of Burn Wounds Using a Handheld Terahertz Hyperspectral Scanner *Adv. Photonics Res.* **3** 2100095
[15] Hernandez-Cardoso G G *et al* 2017 Terahertz imaging for early screening of diabetic foot syndrome: a proof of concept *Sci. Rep.* **7** 42124
[16] Cunningham J, Byrne M B, Wood C D and Dazhang L 2010 On-chip terahertz systems for spectroscopy and imaging *Electron. Lett.* **46** S34–37
[17] Cunningham J E, Byrne M, Upadhya P, Lachab M, Linfield E H and Davies A G 2008 Terahertz evanescent field microscopy of dielectric materials using on-chip waveguides *Appl. Phys. Lett.* **92** 032903
[18] Potts A M, Nayak A K, Nagel M, Kaj K, Stamenic B, John D D, Averitt R D and Young A F 2023 On-Chip Time-Domain Terahertz Spectroscopy of Superconducting Films below the Diffraction Limit *Nano Lett.* **23** 3835
[19] Park S *et al* 2022 Design of a Split Ring Resonator Integrated with On-Chip Terahertz Waveguides for Colon Cancer Detection *Adv. Theory Simul.* **5** 2200313
[20] Nixon J P R, Mosley C D W, Park S J, Wood C D and Cunningham J 2026 Simulated comparison of on-chip terahertz filters for sub-wavelength dielectric sensing *Sensors* **26** 129
[21] Byrne M B, Cunningham J, Tych K, Burnett A D, Stringer M R, Wood C D, Dazhang L, Lachab M, Linfield E H and Davies A G 2008 Terahertz vibrational absorption spectroscopy using microstrip-line waveguides *Appl. Phys. Lett.* **93** 182904
[22] Mosley C D W, Tucker R, Nixon J P R, Park S J, Li L, Freeman J R, Wood C D, Linfield E H, Davies A G and Cunningham J E 2024 Asynchronous optical sampling of on-chip terahertz devices for real-time sensing and imaging applications *Opt. Express* **32** 27940
[23] Dazhang L, Cunningham J, Byrne M B, Khanna S, Wood C D, Burnett A D, Ershad S M, Linfield E H and Davies A G 2009 On-chip terahertz Goubau-line waveguides with integrated photoconductive emitters and mode-discriminating detectors *Appl. Phys. Lett.* **95** 092903
[24] Li D 2010 On-chip pulsed terahertz systems PhD Thesis University of Leeds p 88
[25] Park S J *et al* 2021 Terahertz magnetoplasmon resonances in coupled cavities formed in a gated two-dimensional electron gas *Opt. Express* **29** 12958–66
[26] Russell C *et al* 2013 Spectroscopy of polycrystalline materials using thinned-substrate planar Goubau line at cryogenic temperatures *Lab Chip* **13** 4065–70
[27] Swithenbank M, Burnett A D, Russell C, Li L H, Davies A G, Linfield E H, Cunningham J E and Wood C D 2017 On-Chip Terahertz-Frequency Measurements of Liquids *Anal. Chem.* **89** 7981
[28] Pogue B W and Patterson M S 2006 Review of tissue simulating phantoms for optical spectroscopy, imaging and dosimetry *J. Biomed. Opt.* **11** 041102
[29] Hacker L *et al* 2022 Criteria for the design of tissue-mimicking phantoms for the standardization of biophotonic instrumentation *Nat. Biomed. Eng.* **6** 541
[30] Liakhov E, Smolyanskaya O, Popov A, Odlyanitskiy E, Balbekin N and Khodzitsky M 2016 Fabrication and characterization of biotissue-mimicking phantoms in the THz frequency range *J. Phys.: Conf. Ser.* **735** 012080
[31] Saxena S, Bench C, Garg D, Boardman P, Mrnka M, Penketh H, Stone N and Hendry E 2024 Limitations of effective medium models for tissue phantoms in the THz frequency range *Sci. Rep.* **14** 22968
[32] Yasui T, Saneyoshi E and Araki T 2005 Asynchronous optical sampling terahertz time-domain spectroscopy for ultrahigh spectral resolution and rapid data acquisition *Appl. Phys. Lett.* **87** 061101
[33] GLOphotonics 2025 Specsheet-HCPCF-850-60-v1.03 datasheet
[34] Meng K *et al* 2019 Increasing the sensitivity of terahertz split ring resonator metamaterials for dielectric sensing by localized substrate etching *Opt. Express* **27** 23164
[35] Park S J and Cunningham J 2020 Determination of Permittivity of Dielectric Analytes in the Terahertz Frequency Range Using Split Ring Resonator Elements Integrated with On-Chip Waveguide *Sensors* **20** 4264
[36] Symetrié, 2026 datasheet_solano_2026-1 datasheet
[37] Golda-Cepa M, Engvall K, Hakkarainen M and Kotarba A 2020 Recent progress on parylene C polymer for biomedical applications: a review *Prog. Org. Coat.* **140** 105493
[38] Greenidge N J *et al* 2025 Harnessing the oloid shape in magnetically driven robots to enable high-resolution ultrasound imaging *Sci. Robot.* **10** eadq4198
[39] Mosley C D W *et al* 2026 Data associated with "Sub-wavelength terahertz imaging using asynchronous optical sampling of on-chip near-field sensors" [Dataset] University of Leeds Data Repository (https://doi.org/10.5518/1830)